Research Article Vol. 7, No. 9 / September 2020 / Optica 1181

optica

Nanophotonic supercontinuum-based mid-infrared dual-comb spectroscopy

Hairun Guo,[1,5,†] Wenle Weng,[1,†] Junqiu Liu,[1,†] Fan Yang,[2] Wolfgang Hänsel,[3] Camille Sophie Brès,[4] Luc Thévenaz,[2] Ronald Holzwarth,[3] and Tobias J. Kippenberg[1,*]

[1]Laboratory of Photonics and Quantum Measurements (LPQM), Swiss Federal Institute of Technology Lausanne (EPFL), CH-1015 Lausanne, Switzerland
[2]Group for Fiber Optics (GFO), Swiss Federal Institute of Technology Lausanne (EPFL), CH-1015 Lausanne, Switzerland
[3]Menlo Systems GmbH, 82152 Martinsried, Germany
[4]Photonic Systems Laboratory (PHOSL), Swiss Federal Institute of Technology Lausanne (EPFL), CH-1015 Lausanne, Switzerland
[5]Key laboratory of Specialty Fiber Optics and Optical Access Networks, Joint International Research Laboratory of Specialty Fiber Optics and Advanced Communication, Shanghai Institute for Advanced Communication and Data Science, Shanghai University, Shanghai 200443, China
*Corresponding author: tobias.kippenberg@epfl.ch

Received 29 April 2020; revised 21 July 2020; accepted 27 July 2020 (Doc. ID 396542); published 8 September 2020

High resolution and fast detection of molecular vibrational absorption is important for organic synthesis, pharmaceutical processes, and environmental monitoring, and is enabled by mid-infrared (mid-IR) laser frequency combs via dual-comb spectroscopy. Here, we demonstrate a novel and highly simplified approach to broadband mid-IR dual-comb spectroscopy via supercontinuum generation, achieved using unprecedented nanophotonic dispersion engineering that allows for ultra-broadband and flat-envelope mid-IR frequency combs. Our mid-IR dual-comb spectrometer has an instantaneous bandwidth covering the functional group region from 2800–3600 cm^{-1}, comprising more than 100,000 comb lines, enabling parallel gas-phase detection with a high sensitivity, sub-Doppler spectral resolution, and a high speed. In addition to the traditional functional groups, their isotopologues are also resolved in this supercontinuum-based dual-comb spectroscopy. Our approach combines well established fiber laser combs, digital coherent data averaging, and integrated nonlinear photonics, each in itself a state-of-the-art technology, signaling the emergence of mid-IR dual-comb spectroscopy for use outside of the protected laboratory environment.

https://doi.org/10.1364/OPTICA.396542

1. INTRODUCTION

Mid-infrared (mid-IR) is known as one of the most useful wavelength regions for spectroscopy due to the presence of fundamental vibrational transitions in molecules [1]. Moreover, it has medical potential as human breath contains numerous volatile chemical compounds (VOC), many of which can be associated with diseases [2]. Presently, mid-IR spectroscopy is primarily based on Fourier transform infrared (FTIR) spectrometers [3] that are bulky and have limited resolution and acquisition time. Over the past decade, dual-comb spectroscopy (DCS) has emerged as an approach that can alleviate some of these shortcomings [4,5]. This approach that emerged with the invention of optical frequency combs [6–8] enables fast detection, scanning without moving parts, high resolution spectra, and has no limitation on size, as the device length is independent on resolution, contrary to the FTIR. It is also well known for accessing a broad spectral range yet maintaining a high sensitivity comparable with traditional spectroscopic approaches such as wavelength or frequency modulation spectroscopy [9,10]. DCS has today seen significant advances [11] and has also been successfully applied to an increasing portion of the mid-IR spectrum using a number of mid-IR comb sources [12], including quantum cascade lasers (QCLs) [13], microresonator Kerr frequency combs [14], difference frequency generation (DFG) [15–18], cascaded quadratic nonlinear process [19–23], and optical parametric oscillators (OPO) [24–27]. Yet to date, generating phase locked mid-IR frequency combs that exhibit high brightness, broad bandwidth, and fine resolution remains challenging. The most advanced approaches have used DFG that typically requires the synchronization of two laser beams (even one powerful laser source can be used, it is separated to be one pumping beam and one supercontinuum beam as the probe) and features limited instantaneous spectral bandwidth. To reach a larger spectral coverage, either mechanically tuning the phase matching of the nonlinear crystal or implementing a custom-designed chirped quasi-phase-matching (QPM) is required [17]. OPO-based mid-IR frequency combs have attained some of the broadest spectra to date, allowing for massive parallel sensing of trace molecules [27]. Although capable of a miniature size, this approach is mostly based on solid-state laser cavities that contain discrete bulk optics and components.

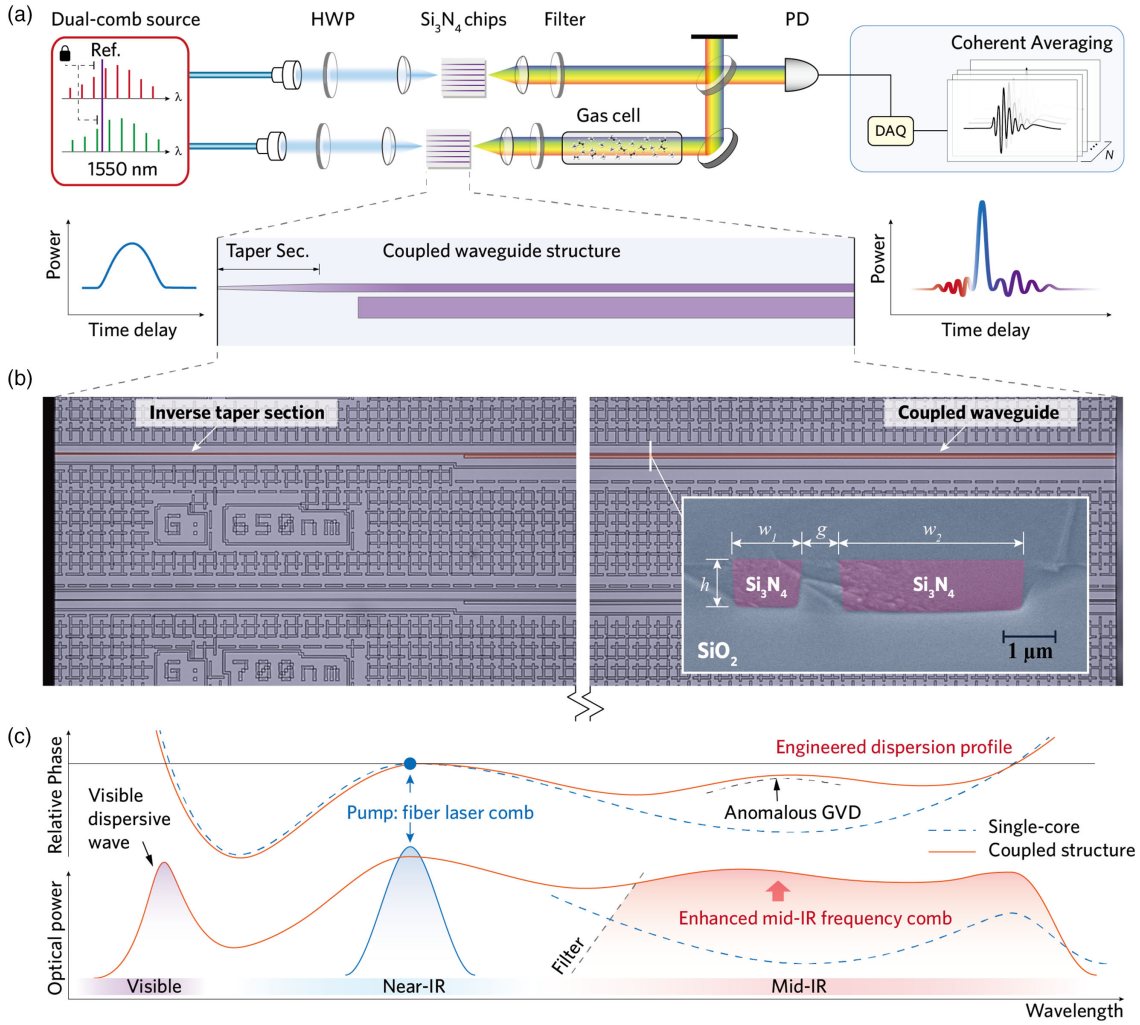

Fig. 1. Nanophotonic supercontinuum-based mid-IR dual-comb spectroscoppy. (a) Schematic setup for mid-IR dual-comb gas-phase spectroscopy, in which two mid-IR frequency combs are generated via coherent supercontinuum process in nanophotonic chip-based Si_3N_4 waveguides, seeded by a mutually locked dual-frequency-comb source at the telecom-band (i.e., ∼1550 nm). HWP, half-wave plate; PD, (mid-IR) photodetector. A schematic of the dual-core Si_3N_4 waveguide, with temporal evolution of the supercontinuum generation, is presented. (b) Microscopic pictures of a photonic integrated chip with coupled Si_3N_4 waveguides, corresponding to both the input section, where the beginning of the waveguide contains an inverse taper structure, and the output section showing dual-core waveguide structures. The false-colored scanning electron microscopic (SEM) picture of the waveguide cross section is also presented. (c) Principle of enhanced mid-IR continuum generation serving as the frequency comb, which corresponds to a dispersion landscape that is engineered and flattened in the mid-IR, particularly by the anomalous GVD produced in the coupled waveguide. Dispersion landscape is defined as relative phase constant compared with the pump pulse, i.e., $\beta(\omega) - \beta_s(\omega)$. In addition, a visible dispersive wave is also supported in this type of waveguide due to the phase matching.

Here, we demonstrate a new approach to mid-IR DCS that offers unprecedented simplicity, based on supercontinuum generation in "coupled" nanophotonic integrated silicon nitride (Si_3N_4) waveguides, and is driven by conventional low-noise fiber-laser-based optical frequency combs in the well developed telecommunication (telecom) band, as shown schematically in Fig. 1. In particular, we propose a coupled waveguide structure that represents an advanced approach to dispersion engineering in the mid-IR, under which the supercontinuum process, seeded in the telecom-band (1550 nm), is along with the mode coupling in the waveguide [Fig. 1(b)] and is tailored to have a large spectral bandwidth and high flatness accessing the mid-IR typically beyond 2500 nm [Fig. 1(c)]. The dual-comb spectrometer we presented offers state-of-the-art signal to noise and large instantaneous spectral bandwidth in the mid-IR (over 800 cm^{-1}). It combines both low-noise fiber lasers and photonic integrated waveguides. Each in itself is a well developed technology, is commercially available, and therefore can contribute to high-performance mid-IR DCS.

2. NANOPHOTONIC SUPERCONTINUUM GENERATION WITH SUPERMODE DISPERSION ENGINEERING

Supercontinuum generation is one of the most dramatic nonlinear optical processes [28] and has been essential for enabling femtosecond lasers to be self-referenced, making fully stabilized optical frequency combs [29]. Fundamentally, it constitutes a way to access ultra-broadband and coherent comb sources and is the key component in DFG for mid-IR frequency comb generation as well as the mid-IR DCS [15,16,30,31]. Recent advances have been

on nanophotonic integrated waveguides, where lithographically tailorable supercontinuum generation is enabled at low pulse energies [32–39], in association with diverse photonic regimes such as QPM [40] and mode perturbation [41,42], and have been applied for laser self-referencing [43,44] and offset frequency detection [37,45] for DFG [46], as well as for spectroscopy [41,47]. In particular, Si_3N_4 waveguides [48], combining a wide transparency with nanophotonic dispersion engineering, have been demonstrated to support mid-IR frequency comb generation based on dispersive wave generation from a femtosecond erbium fiber laser via supercontinuum generation [36,49]. In this way, they provide access to the high-demand mid-IR range by bridging a coherent link with well developed fiber laser technology in the near-infrared (near-IR), amiable for DCS.

The spectral extent and efficiency of supercontinuum generation in nanophotonic waveguides critically depends on the dispersion properties. While the geometry (width and height) of the waveguide can be controlled to achieve dispersion engineering, leading to mid-IR dispersive waves upon the near-IR pump [36], this control poses limitations on achieving a high conversion efficiency and ultra-broadband mid-IR continuum.

Here, we employ coupled structures consisting of multiple Si_3N_4 waveguide cores, typically dual-core waveguides [cf. Fig. 1(b)]. When two waveguide cores are in close proximity, the optical mode propagating in one core is coupled to the other core, which effectively changes its phase, i.e., the propagation constant of the mode ($\beta(\omega)$, where ω is the angular frequency of the light). In this way, the group velocity dispersion (GVD) is also changed as it corresponds to the frequency-dependent phase change induced by the mode coupling ($\mathrm{GVD} = \partial^2\beta/\partial\omega^2$). Physically, mode coupling leads to the hybridization of mode-field distributions, resulting in a pair of supermodes, namely the symmetric and anti-symmetric superpositions of the original uncoupled waveguide modes [50,51]. The coupling induced dispersion (also known as supermode dispersion [52,53]) is then reflected by the phase profile of these supermodes, which is curved to bridge that of the uncoupled modes, and feature an avoided crossing between each other [cf. Fig. 2(a)]. Deterministically, anomalous GVD is always produced by the anti-symmetric mode, while normal GVD is produced by the symmetric mode. In principle, such mode coupling (formally termed "mode hybridization") can be engineered at arbitrary wavelength regions, particularly in the mid-IR, where anomalous GVD is essentially required for dispersion compensation [54] and for tailoring a flattened dispersion profile (with values close to zero over a large bandwidth), but is hardly accessible in conventional single-core waveguides. In detail, the dispersion profile is defined as the relative propagation constant compared with the pump pulse (assumed as temporal soliton):

$$\Delta\beta(\omega) = \beta(\omega) - \beta_s(\omega) \tag{1}$$

$$= \beta(\omega) - (\beta(\omega_s) + v_g^{-1}(\omega - \omega_s)), \tag{2}$$

where $\beta_s(\omega)$ indicates the dispersionless phase profile of the soliton pulse, ω_s is the angular frequency of the pump, and v_g is the soliton group velocity.

Figure 2 illustrates the design of the Si_3N_4 dual-core waveguide. The cross section of the two Si_3N_4 cores are separately selected, in which two modes (one from each core) can feature the hybridization in the mid-IR region, by matching their propagation constants (or equivalently by matching the effective refractive index (n_{eff}), since $\beta = n_{\mathrm{eff}}\omega/c$, where c indicates the speed of light in vacuum). For a choice of Si_3N_4 core widths of $w_1 = 1.3$ μm and $w_2 = 3.4$ μm, respectively, and for an identical core height of $h = 0.85$ μm, two modes, i.e., the fundamental TE_{00} mode in the narrow core and the TE_{10} mode in the wide core, would have the same n_{eff} at the wavelength of 3200 nm [Fig. 2(a)]. Then, for the dual-core waveguide with a coupling gap distance of $g = 0.8$ μm, the propagation constants as well as the mode-field distributions of supermodes are re-calculated. It can be observed that, in the mid-IR where mode hybridization occurs, the propagation constants of supermodes are strongly curved, while in the near-IR away from the hybridization region, they are degenerate to uncoupled modes corresponding to the narrow and wide cores. Therefore, strong and dominant anomalous GVD is induced in the mid-IR from the anti-symmetric modes [at ∼3200 nm, cf. Fig. 2(b)], which is evolved from the narrow core mode in the near-IR. Counterintuitively, the larger change in the supermode dispersion is not achieved by a closer proximity of the two waveguides, as this causes the mode hybridization to occur over a larger spectral range such that the frequency dependency of mode's phase constant is reduced.

A designed dispersion profile of the dual-core waveguide is then shown in Fig. 2(c), which is largely tailored and flattened when compared with that of a conventional single-core waveguide [note that the width of the single-core waveguide is selected such that both waveguides have a similar phase matching ($\Delta\beta(\omega) = 0$) wavelength in the mid-IR for the dispersive wave generation [36,55]].

Significantly, to exploit anomalous GVD in the mid-IR for engineering the supercontinuum, it is imperative to selectively excite the anti-symmetric mode only. This is accomplished by designing the waveguide input section to be the narrow core alone (with an inverse taper in the beginning [56], which efficiently excites the TE_{00} mode), followed by the dual-core section [cf. Fig. 1(b)]. The length of the input section is chosen such that the pulse propagation enters into the dual-core section before significant spectral broadening occurs. Physically, supercontinuum generation is a process that is self-confined in one mode type, where the efficiency of the self-phase modulation (SPM) is maximized. Therefore, being launched into the mode of the narrow core, the near-IR pumping wave upon the supercontinuum process will be self-confined into the anti-symmetric mode and features induced anomalous GVD, when its spectral broadening reaches the hybridization region in the mid-IR.

We next carried out experiments to investigate the supercontinuum generation in the designed Si_3N_4 dual-core waveguides. The waveguides are fabricated using the photonic Damascene process [57], in which thermal annealing steps are critical for reducing the hydrogen content and the related absorption losses [58]. The waveguide length is 5 mm, including the inverse taper section at the beginning. In waveguides similar to the design, supercontinuum generation was observed [Fig. 2(d)], which is seeded by the amplified femtosecond fiber laser in the telecom-band (pulse duration <70 fs, maximum averaged power >350 mW, pulse energy >1 nJ, repetition rate ∼250 MHz). Significantly, with respect to the pumped wavelength (i.e., 1550 nm), the supercontinuum is mostly extended to the long wavelength side, leading to an ultra-broadband mid-IR continuum ranging from 2000–3700 nm, while at the short wavelength side, it features a sharp edge (stopping at 1000 nm) followed by a dispersive wave in the visible range

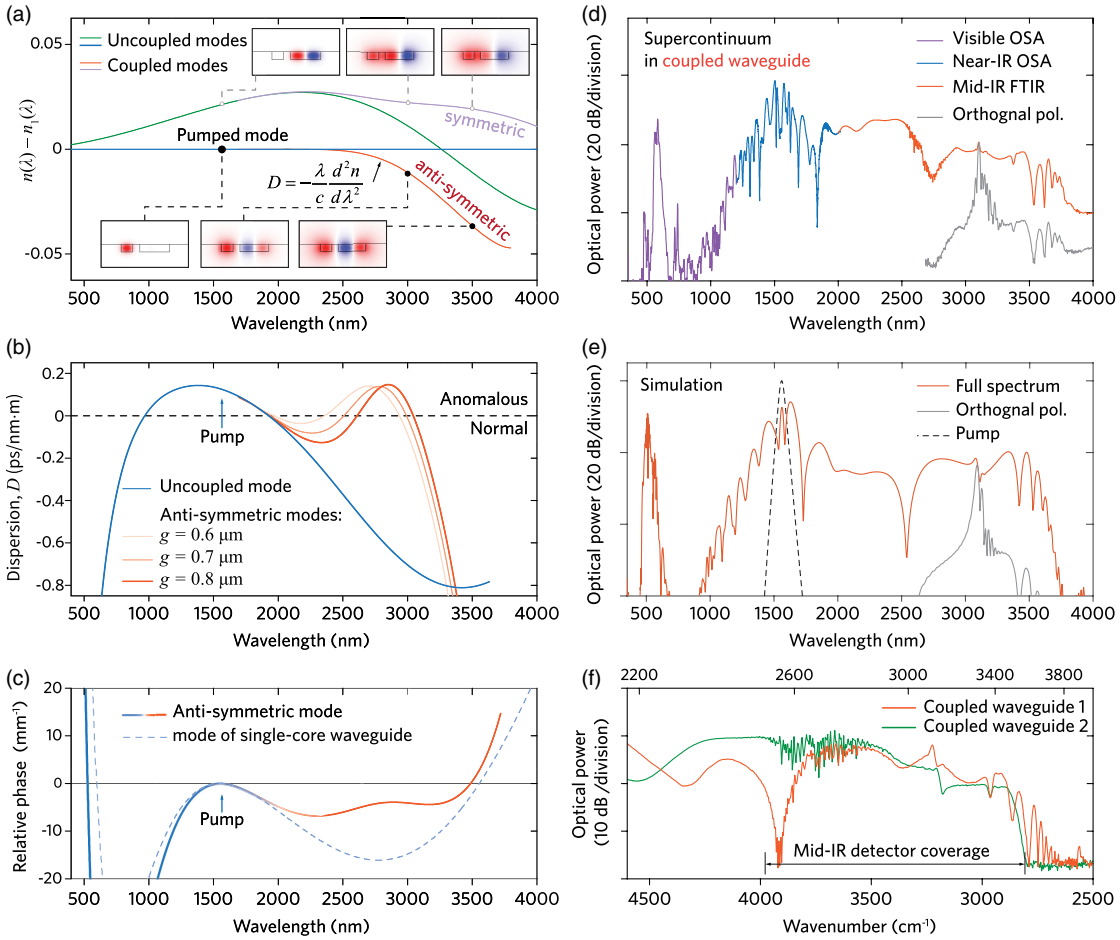

Fig. 2. Design and mid-IR supercontinuum generation in coupled Si_3N_4 waveguides. (a) Calculated effective refractive indices of symmetric (purple curve) and anti-symmetric (orange curve) modes in a dual-core Si_3N_4 waveguide, compared with initial uncoupled modes separated in each core. The geometry of the waveguide is $w_1 = 1.3$ μm, $w_2 = 3.4$ μm, $h = 0.85$ μm, and $g = 0.8$ μm. The mode coupling is between the fundamental TE_{00} mode [marked as $n_1(\lambda)$] in the narrow core (blue curve) and the TE_{10} mode in the wide core (green curve). Insets are the electric-field distribution of the supermodes at different wavelengths. (b) Calculated dispersion (orange curves) of the anti-symmetric mode (corresponding to three gap distances $g = 0.6, 0.7, 0.8$ μm), which produces additional anomalous GVD in the mid-IR compared with the uncoupled mode (blue curve). (c) Calculated dispersion profile of the anti-symmetric mode (with $g = 0.8$ μm) compared with that of a selected single-core waveguide ($w = 1.8$ μm, $h = 0.85$ μm). Both show a similar phase matching wavelength in the mid-IR (ca. 3500 nm). (d) Experimentally observed supercontinuum generation in a dual-core Si_3N_4 waveguide, with measured geometry $w_1 = 1.3$ μm, $w_2 = 3.5$ μm, $h = 0.90$ μm, and $g = 0.65$ μm. OSA, optical spectral analyzers; FTIR, Fourier-transform infrared spectrometer. (e) Simulation of the supercontinuum generation in the dual-core waveguide (cf. Supplement 1 for simulation details). (f) Spectral overlapped two mid-IR supercontinua from two Si_3N_4 chip samples.

(at 600 nm). The spectral envelope exactly reflects the designed dispersion landscape, i.e., the optical power spectrum is inversely proportional to the square of the relative phase constant. Filtering out the mid-IR continuum by an edge-filter (cut-on at 2500 nm), we measured the net power in the mid-IR to be 1–3 mW, depending on the intensity of the pump wave. Note that such a power level already comprises the insertion loss of the waveguide and the loss in the light collecting component (including a mid-IR collecting lens that has a transparency of ~70%), thereby producing sufficient power to implement DCS. The conversion efficiency from the pump wave to the mid-IR frequency comb is estimated to be 1–5%.

In addition, apart from the generation of a flat mid-IR supercontinuum, we also observed a vertically polarized wavelet, i.e., orthogonal to the pump wave that is horizontally polarized, which is narrow-band and comparatively strong in the intensity. This wave is the result of mode coupling between the anti-symmetric mode (TE mode) and a high-order hybrid mode (TM mode) in the dual-core waveguide.

We performed numerical simulations on the supercontinuum process in the dual-core waveguide, see Fig. 2(e), based on two coupled nonlinear Schrödinger equations (cf. Supplement 1 for simulation details), corresponding to the anti-symmetric mode and the high-order mode in the dual-core waveguide. Simulation result shows a high level of agreement with the experiment, in terms of both the supercontinuum envelope and the vertically polarized wavelet in the high-order mode, which confirms that the dual-core waveguide does support a flat mid-IR supercontinuum.

Moreover, we can duplicate the flat mid-IR supercontinuum among separate Si_3N_4 waveguide chips. With a high level of spectral overlap, a broadband mid-IR dual-comb spectrometer is constructed, see Fig. 2(f).

3. NANOPHOTONIC SUPERCONTINUUM-BASED MID-IR DUAL-COMB SPECTROMETER

The schematic setup of the nanophotonic supercontinuum-based mid-IR dual-comb spectrometer is shown in Fig. 1(a). The pump source consists of two ultra-low noise femtosecond fiber lasers with sub-millihertz (mHz) individual linewidth (FC-1500-ULN from Menlo Systems, wavelength ∼1550 nm, repetition rate $f_{rep} \sim 250$ MHz). Both lasers have the carrier-offset frequency locked via self-referencing [7,29], and one comb mode is optically locked to a shared reference laser [at ∼1542 nm, the laser is free-running with a frequency drift of $\mathcal{O}(100$ MHz) over 24 h]. The locked mode index is different by one, which leads to a small difference in the repetition rate, i.e., $\Delta f_{rep} \approx 320$ Hz, and, in principle, allows the dual-comb spectrometer to cover a large span in the optical window, i.e., ∼100 THz (cf. Supplement 1 for detailed analysis on the spectral coverage). In principle, the mid-IR frequency comb from the supercontinuum process is viewed as the spectral extension of the frequency comb structure of the original pump source, therefore it inherits the full properties of the source comb. Based on such a configuration, a phase-resolved mid-IR dual-comb spectrometer was built up, with one mid-IR comb passing through a gas cell for gas-phase detection and the other comb serving as the local reference. After detection, the two combs are interfered on a mid-IR photodetector [VIGO PV-4TE, mercury cadmium telluride (HgCdTe) detector]. In the presence of a difference in the repetition rate, they generate a radio frequency (RF) comb composed of distinguishable heterodyne beats between pairs of optical comb teeth. In the time domain, it corresponds to a periodic interferogram pattern that can be directly recorded by the detector. The data acquisition was implemented by a field programmable gate array (FPGA). The dynamical range is >40 dB supported by sufficient power (>1 mW) in the mid-IR, and by a 16 bit analog-to-digital (ADC) converter embedded in the FPGA. The real-time coherent averaging process [59] is also enabled with a computer for multiple sets of signals (cf. Supplement 1 for details on the coherent averaging process). The normalized signal-to-noise ratio of our spectrometer has a peak value of $25/\sqrt{s}$ at the region of 3400 cm^{-1} (where the spectral intensity is strongest). The typical bandwidth in the mid-IR is $2800 - 3600$ cm^{-1} (∼25 THz), consisting of more than 100, 000 comb elements. The averaged signal-to-noise ratio across this bandwidth is $10/\sqrt{s}$. Therefore, we can conclude a figure of merit of $1.0 \times 10^6/\sqrt{s}$ for our ultra-broadband mid-IR dual-comb spectrometer, which is

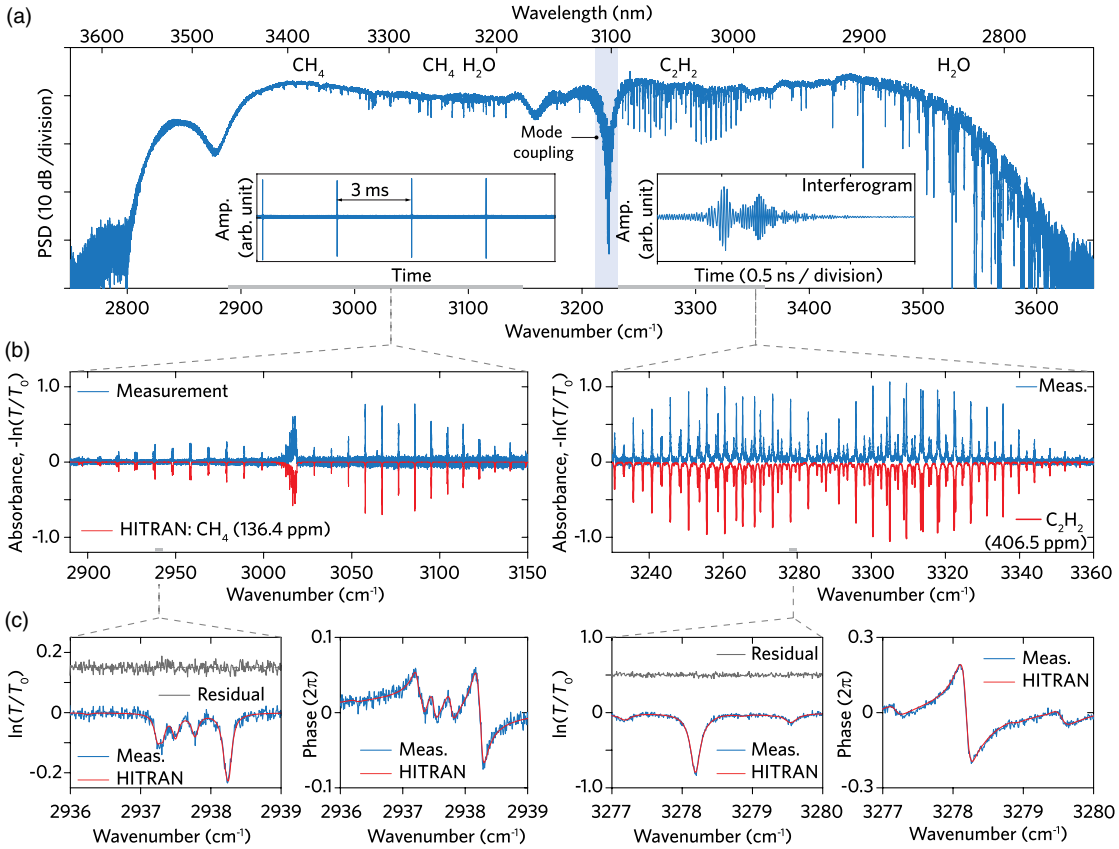

Fig. 3. Parallel gas-phase spectroscopy by mid-IR broadband dual-comb spectrometer. (a) Retrieved mid-IR spectrum from the detected and coherent averaged interferogram trace, after the averaging of 52s (net data acquisition time, cf. Supplement 1 for details on the coherent averaging process), which covers a large span from 2800–3600 cm^{-1}. The gas species in the gas cell, i.e., CH_4 and C_2H_2,g as well as water vapor in the circumstance, are featured as sharp absorbance in the spectrum. Insets show the temporal interferogram trace recorded by the photodetector. The blue shading area marks the mode coupling between the anti-symmetric mode and a higher-order hybrid mode, which exhibits a deep and narrow-band absorption in the spectrum. (b) In this panel, the measured gas absorbance (blue curves), CH_4 (left) and C_2H_2 (right), are fitted and compared with the HITRAN database (red curves, inverted for clarity) within a large span in the spectrum. The gas cell has the total pressure of 1atm, the fitted concentration is CH_4 at 136.4 ppm and C_2H_2 at 406.5 ppm, with nitrogen as the buffer gas. (c) In this panel, detailed gas absorbance, including both the intensity and the phase information, are compared with the HITRAN database. The residual signal from the fitting is also presented, with an offset value (0.15 for CH_4 data and 0.5 for C_2H_2) artificially imposed merely for plotting purpose.

mostly limited by the relative intensity noise (RIN) on the mid-IR frequency combs (cf. Supplement 1 for RIN information). Although this figure of merit does not reach the shot-noise limit, it is comparable to reported results in other works, which for most DFG-based dual-comb spectrometers is from $1-6\times10^{6}/\sqrt{s}$.

4. MID-IR GAS-PHASE SPECTROSCOPIC RESULTS

We next applied the dual-comb spectrometer for mid-IR gas-phase spectroscopy. A gas cell (length 104 cm) was constructed with wedged sapphire windows to avoid etalon effects and filled with a low concentration of methane (CH_4) and acetylene (C_2H_2) as targeted gas samples and nitrogen as the buffer gas. The overall pressure in the cell is 1atm. Figure 3 shows a result of parallel gas detection for both samples. The spectrum [cf. Fig. 3(a)] is retrieved from a coherent averaged temporal interferogram pattern. The averaging time is 52 s. To extract the absorption spectrum, we measure first the spectrum through the gas cell with samples T, then purge the cell, fill it back to the original pressure with pure nitrogen, and measure the reference spectrum T_0. The spectral absorbance is then calculated as $-\ln(T/T_0)$. Due to a limited accuracy in the control of gas pressure as well as the concentration, we made the nonlinear least-square fitting of our measured data with the HITRAN database and left the gas pressure and concentration as floating parameters. These parameters will determine the line intensity and the pressure related collisonal broadening induced linewidth of the absorption spectrum and, by means of the Kramers–Kronig transformation, contribute to reveal the phase spectrum. As a result, the fitted gas pressure and the concentration [cf. Figs. 3(b) and 3(c)] are in good agreement with the measured values, with a relative difference of a few percent that is within the uncertainty level of our gas control instruments. Nevertheless, we noticed that there is a shift on the line center frequency between our measurement and the database, on the order of 100 MHz, which is understood as the underlying frequency instability in the spectrometer (i.e., due to the frequency drift of the reference laser). In addition to gas samples, the concentration of water vapor in the circumstance was also detected as ~1.8%. The normalized and noise limited gas detection sensitivity was estimated to be $\mathcal{O}(10\ \mathrm{ppm}\cdot\mathrm{m}/\sqrt{\mathrm{Hz}})$ (cf. Supplement 1 for detailed analysis on the performance), which is mainly limited by the optical comb power in the mid-IR.

Moreover, the performance of our supercontinuum-based mid-IR DCS was also benchmarked by successful detection of natural isotopologues of CH_4 (Fig. 4), i.e., $^{12}CH_4$, $^{13}CH_4$, and $^{12}CH_3D$. For such a measurement, the gas cell is operated at low pressure such that the collisional broadening of spectral lines is reduced, and those corresponding to isotopologues (i.e., $^{13}CH_4$, natural abundance 1.11%; $^{12}CH_3D$, 0.06%) can be resolved as separated modes from traditional elements ($^{12}CH_4$). In experiments, we set the pressure of the gas cell to be ~0.1atm and the CH_4 concentration to ~12.5%. At this pressure, the full width at half-maximum spectral linewidth of CH_4 is reduced to ~480 MHz, which is both sufficient for distinguishing isotopologues and resolvable by our sub-Doppler resolution (i.e., 250 MHz, determined by the mode spacing) of the mid-IR frequency comb. The capability of identifying a natural abundance of isotopologues is of high importance, as it provides signatures in earth science as well as in cosmology.

5. DISCUSSION

We have demonstrated a high-performance mid-IR dual-comb spectrometer based on the supercontinuum process in nanophotonic integrated nonlinear Si_3N_4 waveguides. The proposed coupled waveguide structure has revealed unprecedented ways of performing dispersion engineering, which can lead to flat-envelope, ultra-broadband mid-IR frequency combs. Such a supercontinuum-based dual-comb spectrometer has not only

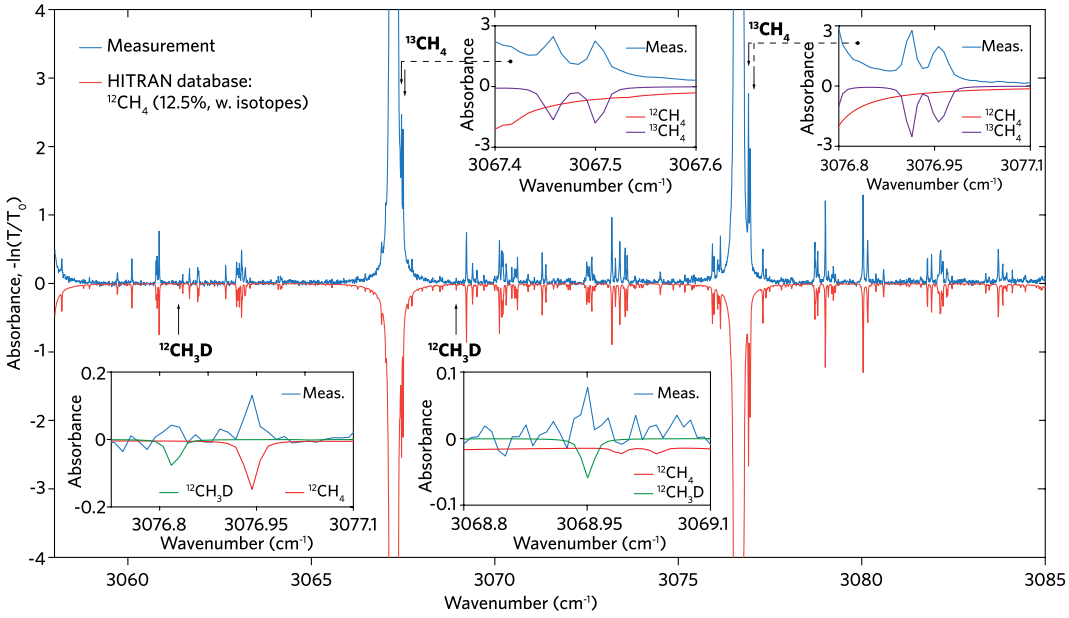

Fig. 4. CH_4 isotopologues resolved by mid-IR dual-comb spectrometer. Measured absorbance of CH_4 (blue curve, averaging time 3.9 s) is compared with the HITRAN database (red curve, inverted for clarity) in the case of high concentration, i.e. ~12.5%. The total pressure of the gas cell is ~0.1atm. Insets show the absorbance of $^{12}CH_4$, $^{13}CH_4$, and $^{12}CH_3D$ at selected regions. Note: for isotopologues such as $^{12}CH_3D$, the noise floor becomes significant, since the absorption signal is very weak. The detection sensitivity remains unchanged.

detected traditional chemical species, but can also trace their isotopologues. Our approach combines fiber laser combs technology with nanophotonic integrated devices, each in itself a well established technology, yet it exhibits a performance competitive to DFG-based dual-comb spectrometers, which is amiable for applications outside the protected laboratory environment. In addition, this approach can benefit from superior laser stabilization methods, e.g., adaptive laser stabilization [60], frequency alignment [61], or feed forward locking [18,62]. At the moment, the long wavelength edge of our spectrometer is limited to 4000 nm (2500 cm^{-1}), which is mostly as a result of the SiO_2 cladding of our Si_3N_4 waveguides. Although Si_3N_4 shows a much larger transparency window reaching the beginning of the backbone region (<2500 cm^{-1}), mode coupling will expose the propagating light mostly to the cladding and therefore feature strong loss in SiO_2. Such a problem can be solved with air-cladding waveguides or substrates that are mid-IR transparent (e.g., sapphire).

Funding. Defense Advanced Research Projects Agency (W31P4Q-16-1-0002); Air Force Office of Scientific Research (FA9550-19-1-0250); Schweizerischer Nationalfonds zur Förderung der Wissenschaftlichen Forschung (163864, 200021_178895); H2020 Marie Skłodowska-Curie Actions (753749); National Natural Science Foundation of China (11974234); Shanghai Science and Technology Development Foundation (20QA1403500); Program for Professor of Special Appointment (Eastern Scholar) at Shanghai Institutions of Higher Learning.

Acknowledgment. The authors acknowledge Miles Anderson for fruitful discussions and suggestions regarding the paper. Nanophotonic Si_3N_4 waveguide chips were fabricated at the Center for MicroNanoTechnology (CMi) at EPFL.

Data Availability. The code and data that support the plots within this paper are available through Zenodo at [63]. All other data and findings of this study are available from the corresponding author upon reasonable request.

Disclosures. H. G., W. W., J. L., and T. J. K. are listed as inventors in a patent application related to this work, filed by EPFL.

See Supplement 1 for supporting content.

[†]These authors contributed equally to the work.

REFERENCES

1. B. Stuart, *Infrared Spectroscopy* (Wiley, 2005).
2. M. Phillips, J. Herrera, S. Krishnan, M. Zain, J. Greenberg, and R. N. Cataneo, "Variation in volatile organic compounds in the breath of normal humans," J. Chromatogr. B **729**, 75–88 (1999).
3. P. R. Griffiths and J. A. De Haseth, *Fourier Transform Infrared Spectrometry* (Wiley, 2007), Vol. **171**.
4. F. Keilmann, C. Gohle, and R. Holzwarth, "Time-domain mid-infrared frequency-comb spectrometer," Opt. Lett. **29**, 1542–1544 (2004).
5. A. Schliesser, M. Brehm, F. Keilmann, and D. W. van der Weide, "Frequency-comb infrared spectrometer for rapid, remote chemical sensing," Opt. Express **13**, 9029–9038 (2005).
6. T. Udem, R. Holzwarth, and T. W. Hänsch, "Optical frequency metrology," Nature **416**, 233–237 (2002).
7. D. J. Jones, S. A. Diddams, J. K. Ranka, A. Stentz, R. S. Windeler, J. L. Hall, and S. T. Cundiff, "Carrier-envelope phase control of femtosecond mode-locked lasers and direct optical frequency synthesis," Science **288**, 635–639 (2000).
8. R. Holzwarth, T. Udem, T. W. Hänsch, J. Knight, W. Wadsworth, and P. St.J. Russell, "Optical frequency synthesizer for precision spectroscopy," Phys. Rev. Lett. **85**, 2264 (2000).
9. E. I. Moses and C. L. Tang, "High-sensitivity laser wavelength-modulation spectroscopy," Opt. Lett. **1**, 115–117 (1977).
10. G. C. Bjorklund, "Frequency-modulation spectroscopy: a new method for measuring weak absorptions and dispersions," Opt. Lett. **5**, 15–17 (1980).
11. I. Coddington, N. Newbury, and W. Swann, "Dual-comb spectroscopy," Optica **3**, 414–426 (2016).
12. A. Schliesser, N. Picqué, and T. W. Hänsch, "Mid-infrared frequency combs," Nat. Photonics **6**, 440–449 (2012).
13. G. Villares, A. Hugi, S. Blaser, and J. Faist, "Dual-comb spectroscopy based on quantum-cascade-laser frequency combs," Nat. Commun. **5**, 5192 (2014).
14. M. Yu, Y. Okawachi, A. G. Griffith, N. Picqué, M. Lipson, and A. L. Gaeta, "Silicon-chip-based mid-infrared dual-comb spectroscopy," Nat. Commun. **9**, 1869 (2018).
15. F. Keilmann and S. Amarie, "Mid-infrared frequency comb spanning an octave based on an Er fiber laser and difference-frequency generation," J. Infrared Millim. Terahertz Waves **33**, 479–484 (2012).
16. F. C. Cruz, D. L. Maser, T. Johnson, G. Ycas, A. Klose, F. R. Giorgetta, I. Coddington, and S. A. Diddams, "Mid-infrared optical frequency combs based on difference frequency generation for molecular spectroscopy," Opt. Express **23**, 26814–26824 (2015).
17. G. Ycas, F. R. Giorgetta, E. Baumann, I. Coddington, D. Herman, S. A. Diddams, and N. R. Newbury, "High-coherence mid-infrared dual-comb spectroscopy spanning 2.6 to 5.2 μm," Nat. Photonics **12**, 202–208 (2018).
18. Z. Chen, T. W. Hänsch, and N. Picqué, "Mid-infrared feed-forward dual-comb spectroscopy," Proc. Natl. Acad. Sci. USA **116**, 3454–3459 (2019).
19. B. Zhou, X. Liu, H. Guo, X. Zeng, X. Chen, H. Chung, Y.-H. Chen, and M. Bache, "Parametrically tunable soliton-induced resonant radiation by three-wave mixing," Phys. Rev. Lett. **118**, 143901 (2017).
20. A. S. Kowligy, A. Lind, D. D. Hickstein, D. R. Carlson, H. Timmers, N. Nader, F. C. Cruz, G. Ycas, S. B. Papp, and S. A. Diddams, "Mid-infrared frequency comb generation via cascaded quadratic nonlinearities in quasi-phase-matched waveguides," Opt. Lett. **43**, 1678–1681 (2018).
21. H. Timmers, A. Kowligy, A. Lind, F. C. Cruz, N. Nader, M. Silfies, G. Ycas, T. K. Allison, P. G. Schunemann, and S. B. Papp, "Molecular fingerprinting with bright, broadband infrared frequency combs," Optica **5**, 727–732 (2018).
22. S. Vasilyev, I. Moskalev, V. Smolski, J. Peppers, M. Mirov, A. Muraviev, K. Vodopyanov, S. Mirov, and V. Gapontsev, "Multi-octave visible to long-wave IR femtosecond continuum generated in Cr:ZnS-GaSe tandem," Opt. Express **27**, 16405–16412 (2019).
23. A. J. Lind, A. Kowligy, H. Timmers, F. C. Cruz, N. Nader, M. C. Silfies, T. K. Allison, and S. A. Diddams, "$\chi^{(2)}$ mid-infrared frequency comb generation and stabilization with few-cycle pulses," arXiv:1811.02604 (2018).
24. B. Bernhardt, E. Sorokin, P. Jacquet, R. Thon, T. Becker, I. T. Sorokina, N. Picqué, and T. W. Hänsch, "Mid-infrared dual-comb spectroscopy with 2.4 μm Cr^{2+}: ZnSe femtosecond lasers," Appl. Phys. B **100**, 3–8 (2010).
25. Z. Zhang, T. Gardiner, and D. T. Reid, "Mid-infrared dual-comb spectroscopy with an optical parametric oscillator," Opt. Lett. **38**, 3148–3150 (2013).
26. Y. Jin, S. M. Cristescu, F. J. Harren, and J. Mandon, "Two-crystal mid-infrared optical parametric oscillator for absorption and dispersion dual-comb spectroscopy," Opt. Lett. **39**, 3270–3273 (2014).
27. A. Muraviev, V. Smolski, Z. Loparo, and K. Vodopyanov, "Massively parallel sensing of trace molecules and their isotopologues with broadband subharmonic mid-infrared frequency combs," Nat. Photonics **12**, 209–214 (2018).
28. J. M. Dudley, G. Genty, and S. Coen, "Supercontinuum generation in photonic crystal fiber," Rev. Mod. Phys. **78**, 1135 (2006).
29. S. T. Cundiff and J. Ye, "Colloquium: femtosecond optical frequency combs," Rev. Mod. Phys. **75**, 325–342 (2003).

30. C. Erny, K. Moutzouris, J. Biegert, D. Kühlke, F. Adler, A. Leitenstorfer, and U. Keller, "Mid-infrared difference-frequency generation of ultrashort pulses tunable between 3.2 and 4.8 μm from a compact fiber source," Opt. Lett. **32**, 1138–1140 (2007).
31. A. Ruehl, A. Gambetta, I. Hartl, M. E. Fermann, K. S. Eikema, and M. Marangoni, "Widely-tunable mid-infrared frequency comb source based on difference frequency generation," Opt. Lett. **37**, 2232–2234 (2012).
32. S. Xie, F. Tani, J. C. Travers, P. Uebel, C. Caillaud, J. Troles, M. A. Schmidt, and P. St.J. Russell, "As_2S_3–silica double-nanospike waveguide for mid-infrared supercontinuum generation," Opt. Lett. **39**, 5216–5219 (2014).
33. B. Kuyken, T. Ideguchi, S. Holzner, M. Yan, T. W. Hänsch, J. Van Campenhout, P. Verheyen, S. Coen, F. Leo, and R. Baets, "An octave-spanning mid-infrared frequency comb generated in a silicon nanophotonic wire waveguide," Nat. Commun. **6**, 6310 (2015).
34. D. Yoon Oh, K. Y. Yang, C. Fredrick, G. Ycas, S. A. Diddams, and K. J. Vahala, "Coherent ultra-violet to near-infrared generation in silica ridge waveguides," Nat. Commun. **8**, 13922 (2017).
35. D. D. Hickstein, H. Jung, D. R. Carlson, A. Lind, I. Coddington, K. Srinivasan, G. G. Ycas, D. C. Cole, A. Kowligy, C. Fredrick, S. Droste, E. S. Lamb, N. R. Newbury, H. X. Tang, S. A. Diddams, and S. B. Papp, "Ultrabroadband supercontinuum generation and frequency-comb stabilization using on-chip waveguides with both cubic and quadratic nonlinearities," Phys. Rev. Appl. **8**, 014025 (2017).
36. H. Guo, C. Herkommer, A. Billat, D. Grassani, C. Zhang, M. H. P. Pfeiffer, W. Weng, C.-S. Brès, and T. J. Kippenberg, "Mid-infrared frequency comb via coherent dispersive wave generation in silicon nitride nanophotonic waveguides," Nat. Photonics **12**, 330–335 (2018).
37. Y. Okawachi, M. Yu, J. Cardenas, X. Ji, A. Klenner, M. Lipson, and A. L. Gaeta, "Carrier envelope offset detection via simultaneous supercontinuum and second-harmonic generation in a silicon nitride waveguide," Opt. Lett. **43**, 4627–4630 (2018).
38. M. Yu, B. Desiatov, Y. Okawachi, A. L. Gaeta, and M. Lončar, "Coherent two-octave-spanning supercontinuum generation in lithium-niobate waveguides," Opt. Lett. **44**, 1222–1225 (2019).
39. B. Kuyken, M. Billet, F. Leo, K. Yvind, and M. Pu, "Octave-spanning coherent supercontinuum generation in an AlGaAs-on-insulator waveguide," Opt. Lett. **45**, 603–606 (2020).
40. D. D. Hickstein, G. C. Kerber, D. R. Carlson, L. Chang, D. Westly, K. Srinivasan, A. Kowligy, J. E. Bowers, S. A. Diddams, and S. B. Papp, "Quasi-phase-matched supercontinuum generation in photonic waveguides," Phys. Rev. Lett. **120**, 053903 (2018).
41. N. Nader, D. L. Maser, F. C. Cruz, A. Kowligy, H. Timmers, J. Chiles, C. Fredrick, D. A. Westly, S. W. Nam, and R. P. Mirin, "Versatile silicon-waveguide supercontinuum for coherent mid-infrared spectroscopy," APL Photon. **3**, 036102 (2018).
42. N. Singh, D. Vermulen, A. Ruocco, N. Li, E. Ippen, F. X. Kärtner, and M. R. Watts, "Supercontinuum generation in varying dispersion and birefringent silicon waveguide," Opt. Express **27**, 31698–31712 (2019).
43. D. R. Carlson, D. D. Hickstein, A. Lind, S. Droste, D. Westly, N. Nader, I. Coddington, N. R. Newbury, K. Srinivasan, and S. A. Diddams, "Self-referenced frequency combs using high-efficiency silicon-nitride waveguides," Opt. Lett. **42**, 2314–2317 (2017).
44. Y. Okawachi, M. Yu, B. Desiatov, B. Y. Kim, T. Hansson, M. Lončar, and A. L. Gaeta, "On-chip self-referencing using integrated lithium niobate waveguides," arXiv:2003.11599 (2020).
45. A. S. Mayer, A. Klenner, A. R. Johnson, K. Luke, M. R. E. Lamont, Y. Okawachi, M. Lipson, A. L. Gaeta, and U. Keller, "Frequency comb offset detection using supercontinuum generation in silicon nitride waveguides," Opt. Express **23**, 15440–15451 (2015).
46. A. S. Mayer, C. R. Phillips, C. Langrock, A. Klenner, A. R. Johnson, K. Luke, Y. Okawachi, M. Lipson, A. L. Gaeta, M. M. Fejer, and U. Keller, "Offset-free gigahertz mid infrared frequency comb based on optical parametric amplification in a periodically poled lithium niobate waveguide," Phys. Rev. Appl. **6**, 054009 (2016).
47. E. Baumann, E. V. Hoenig, E. F. Perez, G. M. Colacion, F. R. Giorgetta, K. C. Cossel, G. Ycas, D. R. Carlson, D. D. Hickstein, K. Srinivasan, S. B. Papp, N. R. Newbury, and I. Coddington, "Dual-comb spectroscopy with tailored spectral broadening in Si_3N_4 nanophotonics," Opt. Express **27**, 11869–11876 (2019).
48. D. J. Moss, R. Morandotti, A. L. Gaeta, and M. Lipson, "New CMOS-compatible platforms based on silicon nitride and Hydex for nonlinear optics," Nat. Photonics **7**, 597–607 (2013).
49. D. Grassani, E. Tagkoudi, H. Guo, C. Herkommer, F. Yang, T. J. Kippenberg, and C.-S. Brès, "Mid infrared gas spectroscopy using efficient fiber laser driven photonic chip-based supercontinuum," Nat. Commun. **10**, 1553 (2019).
50. A. Yariv, "Coupled-mode theory for guided-wave optics," IEEE J. Quantum Electron. **9**, 919–933 (1973).
51. E. Marom, O. Ramer, and S. Ruschin, "Relation between normal-mode and coupled-mode analyses of parallel waveguides," IEEE J. Quantum Electron. **20**, 1311–1319 (1984).
52. U. Peschel, T. Peschel, and F. Lederer, "A compact device for highly efficient dispersion compensation in fiber transmission," Appl. Phys. Lett. **67**, 2111–2113 (1995).
53. Y. Lee, "Pulse compression using coupled-waveguide structures as highly dispersive elements," Appl. Phys. Lett. **73**, 2715–2717 (1998).
54. Y. Bidaux, F. Kapsalidis, P. Jouy, M. Beck, and J. Faist, "Coupled-waveguides for dispersion compensation in semiconductor lasers," Laser Photon. Rev. **12**, 1700323 (2018).
55. N. Akhmediev and M. Karlsson, "Cherenkov radiation emitted by solitons in optical fibers," Phys. Rev. A **51**, 2602 (1995).
56. J. Liu, A. S. Raja, M. H. P. Pfeiffer, C. Herkommer, H. Guo, M. Zervas, M. Geiselmann, and T. J. Kippenberg, "Double inverse nanotapers for efficient light coupling to integrated photonic devices," Opt. Lett. **43**, 3200–3203 (2018).
57. M. H. P. Pfeiffer, A. Kordts, V. Brasch, M. Zervas, M. Geiselmann, J. D. Jost, and T. J. Kippenberg, "Photonic Damascene process for integrated high-Q microresonator based nonlinear photonics," Optica **3**, 20–25 (2016).
58. J. Liu, A. S. Raja, M. Karpov, B. Ghadiani, M. H. P. Pfeiffer, B. Du, N. J. Engelsen, H. Guo, M. Zervas, and T. J. Kippenberg, "Ultralow-power chip-based soliton microcombs for photonic integration," Optica **5**, 1347–1353 (2018).
59. I. Coddington, W. Swann, and N. Newbury, "Coherent dual-comb spectroscopy at high signal-to-noise ratio," Phys. Rev. A **82**, 043817 (2010).
60. T. Ideguchi, A. Poisson, G. Guelachvili, N. Picqué, and T. W. Hänsch, "Adaptive real-time dual-comb spectroscopy," Nat. Commun. **5**, 3375 (2014).
61. G. Millot, S. Pitois, M. Yan, T. Hovhannisyan, A. Bendahmane, T. W. Hänsch, and N. Picqué, "Frequency-agile dual-comb spectroscopy," Nat. Photonics **10**, 27–30 (2016).
62. Z. Chen, M. Yan, T. W. Hänsch, and N. Picqué, "A phase-stable dual-comb interferometer," Nat. Commun. **9**, 3035 (2018).
63. H. Guo, W. Weng, J. Liu, F. Yang, W. Hänsel, C. S. Brés, L. Thévenaz, R. Holzwarth, and T. J. Kippenberg, Zenodo, 2020, https://doi.org/10.5281/zenodo.3986965